S1 Signal processing and data analysis for the ERICA-AMS

S1.1 Signal preparation and analysis

The ionized vapour is extracted by an extraction pulser working at a frequency of $50\,\text{kHz}$, resulting in a maximum m/z of above 700. The data acquisition card averages 20 000 extractions to one raw spectrum that is then transmitted to the computer and represents $0.4\,\text{s}$ of measurement. One measurement cycle of the ERICA-AMS consists of $10\,\text{s}$ or 25 raw spectra. 12 raw spectra ($4.8\,\text{s}$) are taken while the shutter is open as representative for the aerosol measurement, whereas during 11 raw spectra ($4.4\,\text{s}$) the shutter is closed for a background measurement (i.e. residual vacuum signal). Two raw spectra ($0.8\,\text{s}$) are needed for the switching of the shutter and are discarded due to an undefined shutter position. One data file is recorded every five minutes. A sudden power interrupt prohibits the finalization of the data file, thus the last file of the flight is usually corrupted. In TofWare 2.5.7 we adjusted the settings to comply with the ERICA-AMS data. Executing *"setigoroption poundde-fine= tw_ACSM_diffSticks_dontNorm28"* and recompiling as well as activating the button *"Background is blocked beam (adv)"* prevents TofWare from normalization of each spectrum to m/z 28. This normalization is only practical in ACSM instruments, which the software was designed for. Due to our inhouse-built shutter unit, the software is unable to read the shutter position, thus we set it manually to $1-12$ (Total) and $14-24$ (Bkgnd), switch buf 13. The triggering of the shutter directly by the ADQ precludes potential shifts in the time scheme. We also insert the IE calibration factor (cf. section S1.2) and the sample flow rate into the instrument as measured with a Gilibrator (i.e. a value of $1.45\,\text{cm}^3\text{s}^{-1}$). In order to convert the raw spectra into an integrated unit mass resolution (UMR) spectrum, also called stick spectrum, an m/z calibration is needed to identify the signal peaks. We use a three-parameter fit of the form $p_1 \cdot m^{p_3} + p_2$ to the masses of CH^+ ($m/z = 13.0078$), O_2 (31.9898), SO_2 (63.9619), ^{182}W (181.948), ^{184}W (183.951) and ^{186}W (185.954). A time series of calibration values for each data point was used. TofWare calculates a time series of stick spectra according to the predefined values. The aerosol signal is represented by the "diff" spectrum, which is the difference of the measurement with an open shutter and a closed shutter. After excluding 16 data points as outliers and 1289 data points acquired during cloud passes (about $11.7\,\%$ of the data) the data basis for this publication is 9624 data points, $10\,\text{s}$ each, resulting in a total of $26\,\text{h}$ and $44\,\text{min}$ of measurement time over all eight scientific flights.

S1.2 IE calibrations for StratoClim and fragmentation table

The conversion of the measured signal into a particle mass concentration is achieved by an ionization efficiency (IE) calibration implemented as the mass-based or bulk method (e.g. Drewnick et al., 2005). Therefore a polydisperse aerosol of a known substance (ammonium nitrate or ammonium sulfate) is generated by a nebulizer. A differential mobility analyzer (DMA) is used to select particles of a defined electromobility diameter. The particle number concentration measured by a condensation particle counter and the particle diameter are then used to calculate the total particulate mass concentration introduced into the instrument. By comparison with the acquired signal on the ERICA-AMS data acquisition card and the previously determined signal of single ions with the Software *"SingleIon2"* (TofWerk), the ionization efficiency of nitrate and the ionization efficiency relative to nitrate (RIE) of ammonium and sulfate is determined. Averaged over four calibrations, we found an IE calibration factor of $1965\,\text{ions}\,\text{pg}^{-1}$, $RIE(NH_4) = 4.37$ and $RIE(SO_4) = 0.97$ to be valid for flights 1 and 4-8. The calibration values for flight 2 and 3 are based on one measurement with different settings and can be found in Table S1.

The attribution of the UMR signals to the chemical species of interest (e.g. nitrate, organic, ammonium, sulfate) is done by means of a so-called fragmentation table (Allan et al., 2004). Due to the large uncertainty of the mass peaks at m/z 16 and 29 concomitant with the relatively large air beam signal, the fragmentation table had to be modified for the ERICA-AMS. The ammonium signal at m/z 16 is not measured directly, but calculated out of the ammonium signal at m/z 17 using the fragmentation ratio $R_{16/17}$ determined during calibration (see Table S1). The organic signal at m/z 29 is assumed equal to the organic signal at m/z 43. This assumption is based on Fry et al. (2018), who introduced a correction to the nitrate signal for environments with high biogenic contribution to the organic mass concentration as well as low nitrate concentrations in their supplemental material. The correction can accordingly be based on the organic signal at m/z 29 or 43 using the same correction factor. Also the correct contribution of gaseous CO_2 to m/z 44 has to be considered, especially since the particulate organic signal at m/z 44 ($org44$) is crucial for the analysis of photo-oxidation state (see Section S1.6). Since small errors have

Table S1. IE calibrations relevant for the data set of this work

Date (YY-MM-DD)	calib. factor	RIE (NH_4)	RIE (SO_4)	$R_{16/17}$
17-06-29	1883	4.42	1.07	0.83
17-07-28	1956	4.36		0.79
17-09-08	2005	4.38	0.91	0.83
17-09-08	2014	4.31	0.93	0.83
avg	1965	4.37	0.97	0.82
calibration for flight 2 and 3				
17-07-28	1366	4.59	0.67	0.89

more severe consequences at low concentrations rather than at higher concentrations, we decided to adjust the level of $org44$ and organic to be zero at the highest potential temperatures above 460 K. While possibly leading to small errors at different conditions of instrument temperature and CO_2 levels, it is a good proxy for the quantification of small levels of organics found between 420 K and 440 K. We have also tried to estimate the CO_2 levels from filter measurements on the ground, which
50 however lead to unreasonably low and even negative $org44$ and $organic$ levels in the stratosphere.
The collection efficiency of the vaporizer is depending on e.g. the chemical constituents of the aerosol particle. Middlebrook et al. (2012) developed a method to estimate the collection efficiency based on the measured chemical composition. We used this method to correct the acquired mass concentrations, since a high ammonium nitrate fraction as well as very acidic aerosol can be found in the ATAL and lower stratosphere, respectively. Both can lead to a significantly higher collection efficiency than
55 the commonly assumed 0.5 (Allan et al., 2003a).

S1.3 Determination of the detection limit

To distinguish between aerosol signals and the noise level the lower detection limit of the ERICA-AMS has to be determined. While several methods are described in the literature, e.g. estimation from a reference measurement with particle free air through a HEPA filter (Allan et al., 2003b; Bahreini et al., 2003), from the background measurement (Drewnick et al., 2009)
60 or the ion counting statistics (Allan et al., 2003b), these methods show significant downsides during airborne AMS operation. The determination of the noise during a filter measurement is only representative for a distinct time period of the flight, since vacuum background and temperature vary over time. The variation of the background measurement also cannot be used as a proxy for the noise, because most of the variation of the background signal is due to the vacuum which improved with flight time or varying temperatures rather than statistical noise.
65 We describe the background signal as

$$F(t) = T(t) + N(t) \tag{1}$$

where $T(t)$ denotes the trend due to improving vacuum or varying temperature and $N(t)$ describes the time dependent random noise, where the standard deviation over an arbitrary number of points n is given by

$$\sigma = \sqrt{\frac{\sum_n N(t)^2}{n}}. \tag{2}$$

70 The Savitzki-Golay filter (Savitzky and Golay, 1964) is a method for random noise reduction, and we used a third order smoothing over $m = 5$ data points resulting in a smoothed background signal

$$F_{smoothed}(t) = T(t) + N_{red}(t) \tag{3}$$

with reduced noise $N_{red}(t)$. The reduced noise shows a standard deviation of (Ziegler, 1981)

$$\sigma_{red} = \sqrt{\frac{\sum_n N_{red}(t)^2}{n}} = \sqrt{\frac{3 \cdot (3m^2 - 7)}{4m \cdot (m^2 - 4)}} \cdot \sigma = \sqrt{\frac{17}{35}} \cdot \sigma. \tag{4}$$

Still, $T(t)$ and $N_{red}(t)$ remain unknown. However, we can calculate the difference function

$$D(t) = F(t) - F_{smoothed}(t) = N(t) - N_{red}(t) \tag{5}$$

which consists of noise functions with an expectation value of 0, each. The standard deviation σ of the original noise function $N(t)$ then represents the convolution of $\sigma_{red} = \sqrt{\frac{17}{35}} \cdot \sigma$ and $\sigma_D = \sqrt{\frac{\sum_n D(t)^2}{n}}$, leading to the equation

$$\sigma^2 = \sigma_{red}^2 + \sigma_D^2 = \frac{35}{18} \cdot \sigma_D^2. \tag{6}$$

By calculating $\sigma_D = \sqrt{\frac{\sum_n D(t)^2}{n}}$, we thus know the magnitude of the standard deviation $\sigma = \sqrt{\frac{35}{18}} \cdot \sigma_D$ of the background noise, despite of not being able to remove the noise.

The detection limit is then given by $3 \cdot \sigma$ in agreement with Allan et al. (2003b), Bahreini et al. (2003) and Drewnick et al. (2009). A similar method to determine the detection limit of a signal containing a trend has been introduced by Reitz (2011) and applied by Schulz et al. (2018). A comparison with detection limits calculated from the filter method based on lab measurements proves the validity of this method (Schulz, 2019; Hünig et al., 2021).

S1.4 Chloride signal in the ERICA-AMS during the Stratoclim 2017 aircraft campaign

During the StratoClim campaign we observed the chloride signal to be smaller than the detection limit even after averaging over up to two hours of flight time at the same altitude level. Detectable amounts of particulate chloride were only found inside the boundary layer, which is not subject of this publication. Chloride has been excluded from the analysis of this study, including total mass, mass fraction, acidity balance.

S1.5 Temperature dependence of the ERICA-AMS signal

The signal of the air beam strongly varied during each flight by up to $40\,\%$. We found the signal to increase with decreasing temperature inside the pressurized barrel. Lab experiments with a selective heating of different components showed a dependence of the signal with the temperature of the MCP, whereas heating or cooling of other instrument components (sample air inlet, signal amplifiers, HV generator, data acquisition card) showed much less influence on the detected signal. We conclude that the variation of the air beam signal is caused by the temperature dependence of the MCP gain as was previously examined by Siddiqui (1979) and Slater and Timothy (1993). The signal dependence on temperature affects the aerosol signal the same way as the air beam. We therefore corrected all data according to this variation, commonly known as air beam correction (Allan et al., 2003b).

S1.6 Analysis of the oxidation state of organics

Among the common species - organics, nitrate, ammonium, sulfate, and chloride - the fragmentation table can also be used to generate signals of species at a specific m/z. For example, $org43$ and $org44$ are the contributions of m/z 43 and 44, respectively, to the total organic signal (denoted as "organics"). The relative contribution to the organic signal is $f_{43} = \frac{org43}{organics}$ and $f_{44} = \frac{org44}{organics}$. Ng et al. (2010) showed, that these fractions indicate the oxidative ageing of organic aerosols. A high value of f_{43} (resulting mainly from $C_2H_3O^+$ ions) indicate fresh organics, while oxidative ageing leads to an increasing contribution

of organic acids, which results in a higher value of f_{44} (mainly CO_2^+ ions). The values for f_{44} are plotted against f_{43} for each data point of the StratoClim campaign (Fig. 11 in the main paper). We averaged the data over $90\,s$ and only displayed values where the total organic signal as well as the organic signals at m/z 43 and 44 are above the detection limit. The median values and interquartiles for different ranges of potential temperature are indicated by black rectangular boxes. Here all those data points were considered as valid, where the total organics signal was above the detection limit. The lines of the black triangle indicate the region, where the majority of ambient organic aerosol can be found (Ng et al., 2010). Data points in the lower part of the triangle indicate fresh and primary aerosol (Ng et al., 2011). The closer the data point tend to the upper left corner, the higher is the photooxidative ageing of the aerosol.

An additional measure for the photooxidative state can be expressed by the fraction $R_{44/43} = \frac{f_{44}}{f_{43}}$. Here, higher photooxidative states result in a higher value of $R_{44/43}$. $R_{44/43}$ is displayed against altitude and θ in Fig. 14 in the main paper.

S2   Signal processing and data analysis for the ERICA-LAMS

S2.1   Particle classification

The ERICA-LAMS bipolar spectra of single particles are recorded in four channels (two channels of different full scale range for each polarity). The recorded spectra in the four channels are combined into two spectra, one for each polarity. In total, 109,453 particles were chemically analyzed by the ERICA-LAMS during the StratoClim research flights when sampling outside clouds. Of all collected spectra 92 % were dual polarity, and 99 % include particle size information. We applied the separation between measurements inside and outside clouds, since the aerosol inlet was not suited to conduct measurements inside clouds. CDP data were used to separate between the two events, as explained in Sect. 2.

We used the CRISP software package (Concise Retrieval of Information from Single Particles; Klimach, 2012) to perform m/z calibration of mass spectra and peak area integration. The CRISP software package was further used to classify the spectra into different particle types. For particle classification, we combined two commonly used methods: the fuzzy c-means clustering (e.g. Hinz et al., 1999; Roth et al., 2016; Schneider et al., 2021) and the marker ion method (Köllner et al., 2017, 2021). The applied clustering and markering conditions and parameters are summarized in Tables S2 and S3.

In a first step, we applied fuzzy c-means clustering (Clustering 1, see Table S2) according to Schneider et al. (2021) to identify particles containing meteoric material. With the remaining spectra, we repeated fuzzy c-means clustering (Clustering 2, 3, 4, see Table S2) to identify elemental carbon (EC) particles. In a next step, the marker ion method was used to classify the remaining spectra. We examined, if one of the following marker species was included in the single particle spectra, which means, if the respective ion markers were above the ion peak area threshold: K, Si, P, Na, Mg, V, Fe, Ca, Cr, Ti, Cu, Li, Pb, Hg, and Zn (Table S3). The ion peak area threshold for the ERICA-LAMS data during StratoClim 2017 is $7\,mV \cdot sample$ for both polarities (Hünig et al., 2021). 1 sample of the data acquisition card corresponds to $1.6\,ns$. So far, our aim was to identify particles including primary components, i.e. meteoric material, EC, anthropogenic metals, and minerals. As a result, we summed up all particles containing primary components, providing the so-called primary or mixed particle type.

In a final step, we analysed the remaining particles for particle spectra with dominant ion markers at m/z +12, +24, +36, +48 (C_{1-4}^+), and +39 (K^+) (the so-called Low EC/OC particle type) in the StratoClim 2017 data set. We found 5235 particles of this type (out of 109 453). However, it is not clear if this particle type implies the presence of (aged) EC and/or organic carbon (OC) (e.g. Moffet and Prather, 2009; Healy et al., 2009; Zanatta et al., 2019), both mixed with potassium. Hence, the origin of low EC/OC needs further investigation. For this reason, we classified this particle type as "Unidentified" and excluded this particle type from the further analysis.

Besides the mixed and the "unidentified" particle type, we obtained a particle type that consists of all remaining spectra and is characterized by the sole presence of secondary components in single particle spectra (the so-called secondary particle type). We further sorted the secondary type into type 1, showing a dominant peak at m/z 30, and type 2, showing other peaks to be larger than m/z 30. We further sub-divided the secondary particle type in a type 1 with dominant m/z 30 peak and a class with non-dominant m/z 30 peak. For the latter class, other components like ammonium and C_n-structure are dominant.

Table S2. Particle classification by fuzzy c-means clustering. Parameters for the different clustering steps used for the analysis are given. The respective particle types and numbers are shown.

Step	Ion type	Preprocessing	Normalization	Distance metric	Initialization Startcluster Number/Difference	Fuzzifier/Fuzzy abort	Particle type / number characterized by...
Clustering 1[1] of 102,009 dual-polarity spectra	Cation	power each m/z by 0.5	Sum	Correlation	20 / 0.9	1.3/1e-5	1) Meteoric particle / 18467 Dominant m/z +24/25/26 (Mg^+) and +54/56 (Fe^+) 2) Dominant Na^+,K^+,Fe^+ / 934
Clustering 2[2] of 82,608 dual-polarity spectra	Anion+Cation	power each m/z by 0.5	Sum	Correlation	20 / 0.7	1.3/1e-5	3) Elemental Carbon (EC) / 2534 m/z +12,+24,...,+132 (C^+_{1-11}) and m/z -24,-36...,-108 (C^-_{2-9})
Clustering 3[2] of 80,074 dual-polarity spectra	Anion+Cation	power each m/z by 0.5	Sum	Correlation	40 / 0.7	1.3/1e-5	3) Elemental Carbon (EC) / 90 m/z +12,+24,...,+84 (C^+_{1-7}) and m/z -24,-36...,-72 (C^-_{2-6})
Clustering 4[2] of 108 single anion spectra	Anion	power each m/z by 0.5	Sum	Correlation	5 / 0.7	1.3/1e-5	3) Elemental Carbon (EC) / 9 m/z -24,-36...,-132 (C^-_{2-11})

Given reference numbers are defined as follows: [1]Schneider et al. (2021), [2]Roth (2014).

Table S3. Particle classification by marker species and associated ion markers applied in this study.

Marker species	Ion markers
Potassium (K)	m/z +39/41 (K^+)
Silicon (Si)	m/z +28 (Si^+) and m/z -60 (SiO_2^-) and -76 (SiO_3^-)
Phosphorus (P)	m/z -63 (PO_2^-) and -79 (PO_3^+)
Sodium (Na)	m/z +23 (Na^+)
Magnesium (Mg)	m/z +24/25/26 (Mg^+)
Vanadium (V)	m/z +51 (V^+) and +67 (VO^+)
Iron (Fe)	m/z +54/56 (Fe^+)
Calcium (Ca)	m/z +40 (Ca^+)
Chromium (Cr)	m/z +52/53 (Cr^+) and +68 (CrO^+) and +84 (CrO_2^+)
Titanium (Ti)	m/z +48 (Ti^+) and +64 (TiO^+)
Copper (Cu)	m/z +63/65 (Cu^+)
Lithium (Li)	m/z +7 (Li^+)
Lead (Pb)	m/z +206/207/208 (Pb^+)
Mercury (Hg)	m/z +199/200/202 (Hg^+)
Zinc (Zn)	m/z +64/66/68 (Zn^+)
Low elemental or organic carbon (Low EC/OC)	dominant m/z +12,+24,+36,+48 (C_{1-4}^+) and dominant m/z +39 (K^+)

S2.2   Uncertainty analysis

ERICA-LAMS particle number concentration at the first detection stage (N_0)

The absolute uncertainty of the averaged ERICA-LAMS particle number concentration at the first detection stage for each bin ($\sigma_{N_0}^{\text{abs}}$) is calculated based on Poisson statistics:

$$\sigma_{N_0}^{\text{abs}} = N_0 \cdot \sigma_{N_0}^{\text{rel}}, \tag{7}$$

with the $\sigma_{N_0}^{\text{rel}}$ that is defined as follows:

$$\sigma_{N_0}^{\text{rel}} = \frac{1}{\sqrt{C_0}}, \tag{8}$$

with the averaged ERICA-LAMS particle counts at the first detection stage for each bin (C_0).

ERICA-LAMS particle fraction (PF)

The absolute uncertainty of the ERICA-LAMS particle fraction for each bin (σ_{PF}^{abs}) is calculated using binomial statistics:

$$\sigma_{PF}^{\mathrm{abs}} = \frac{\sqrt{N_{\mathrm{hits}} \cdot PF \cdot (1 - PF)}}{N_{\mathrm{hits}}}, \tag{9}$$

with the number of particles that are successfully ionized by the desorption laser and create a mass spectrum (N_{hits}) and the PF.

ERICA-LAMS scaled number concentration ($PF \cdot N_0$)

The absolute uncertainty of the ERICA-LAMS scaled number concentration for each bin ($\sigma_{PF \cdot N_0}^{\mathrm{abs}}$) is calculated using Gaussian propagation of uncertainties:

$$\sigma_{PF \cdot N_0}^{\mathrm{abs}} = \sqrt{\left(PF \cdot \sigma_{N_0}^{\mathrm{abs}}\right)^2 + \left(N_0 \cdot \sigma_{PF}^{\mathrm{abs}}\right)^2}. \tag{10}$$

S3 Additional figures

In Fig. S1 the mass concentration profiles of organics and nitrate are compared. A Gaussian fit shows, that the profile of organic has its mode about 5 K higher and is about 10 K broader ($1/\sqrt{e}$ full width) compared the the nitrate profile of the ATAL.

	organic	nitrate	
amplitude	0.82(3)	0.79(5)	µg m^{-3}
mode	387(1)	382(1)	K
width	39(2)	29(2)	K
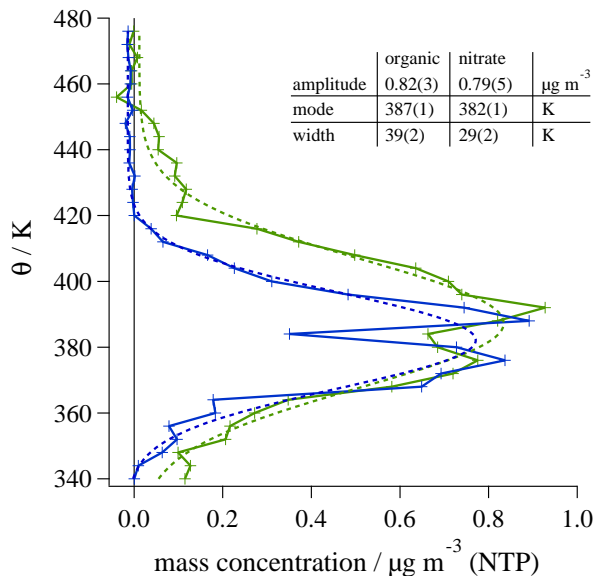
Figure S1. Gaussian fit to the vertical distribution of nitrate and organic mass concentrations, showing the lower edge is similar, but organics reach higher. The width parameter represents the $1/\sqrt{e}$ full width (2σ).

S3.1 Profiles of each flight

The vertical profile measured during each measurement flight is displayed in Fig. S2 to Fig. S9 against GPS altitude and potential temperature θ as reference for further studies.
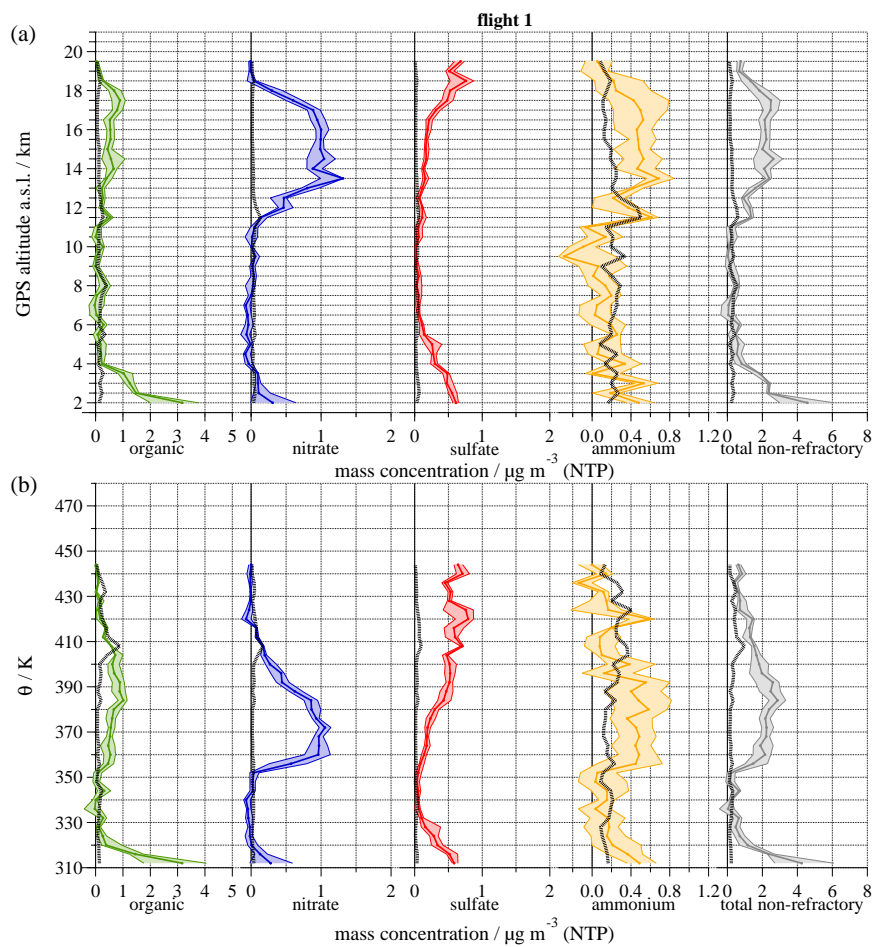
Figure S2. ERICA-AMS mass concentrations of particulate organics (green), nitrate (blue), sulfate (red), and ammonium (NH_4, orange) as a function of (a) GPS altitude and (b) potential temperature θ measured during research flight 1 on 27 July. The thick line and the shaded area represent the median and $25th/75th$ percentiles in the corresponding altitude or θ bin. The right panel displays the sum of all species measured by the ERICA-AMS (grey). For each altitude bin the detection limit is displayed as a dotted line.
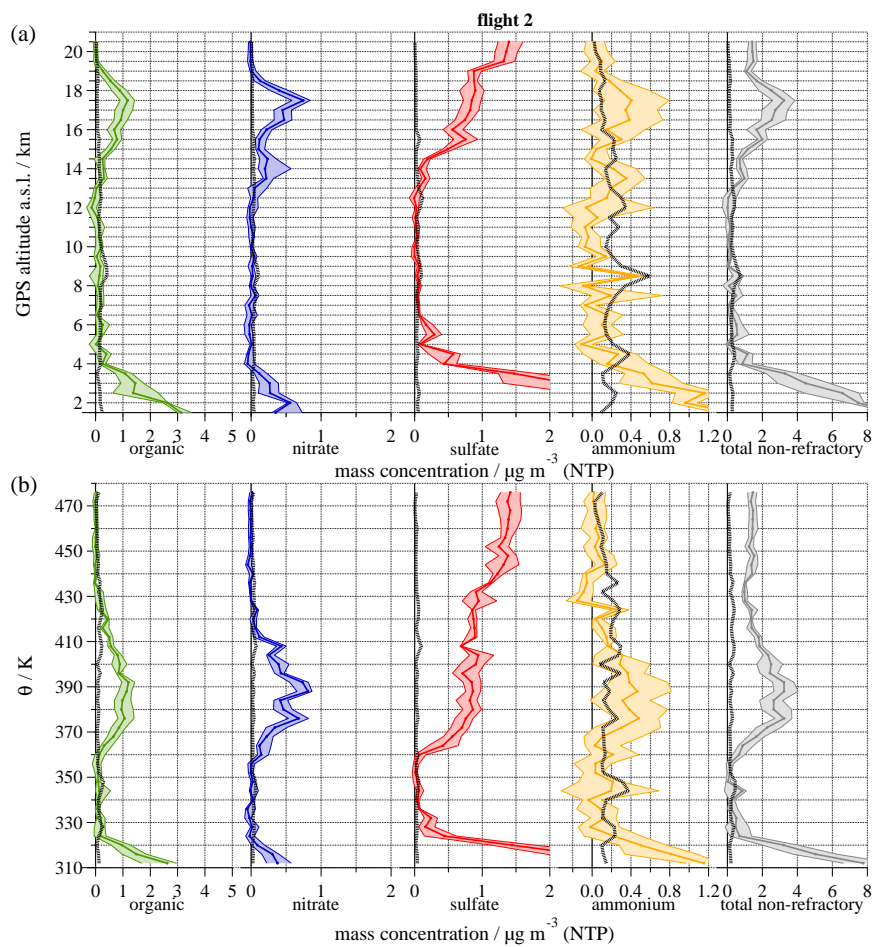
Figure S3. ERICA-AMS mass concentrations of particulate organics (green), nitrate (blue), sulfate (red), and ammonium (NH_4, orange) as a function of (a) GPS altitude and (b) potential temperature θ measured during research flight 2 on 29 July. The thick line and the shaded area represent the median and $25th/75th$ percentiles in the corresponding altitude or θ bin. The right panel displays the sum of all species measured by the ERICA-AMS (grey). For each altitude bin the detection limit is displayed as a dotted line.
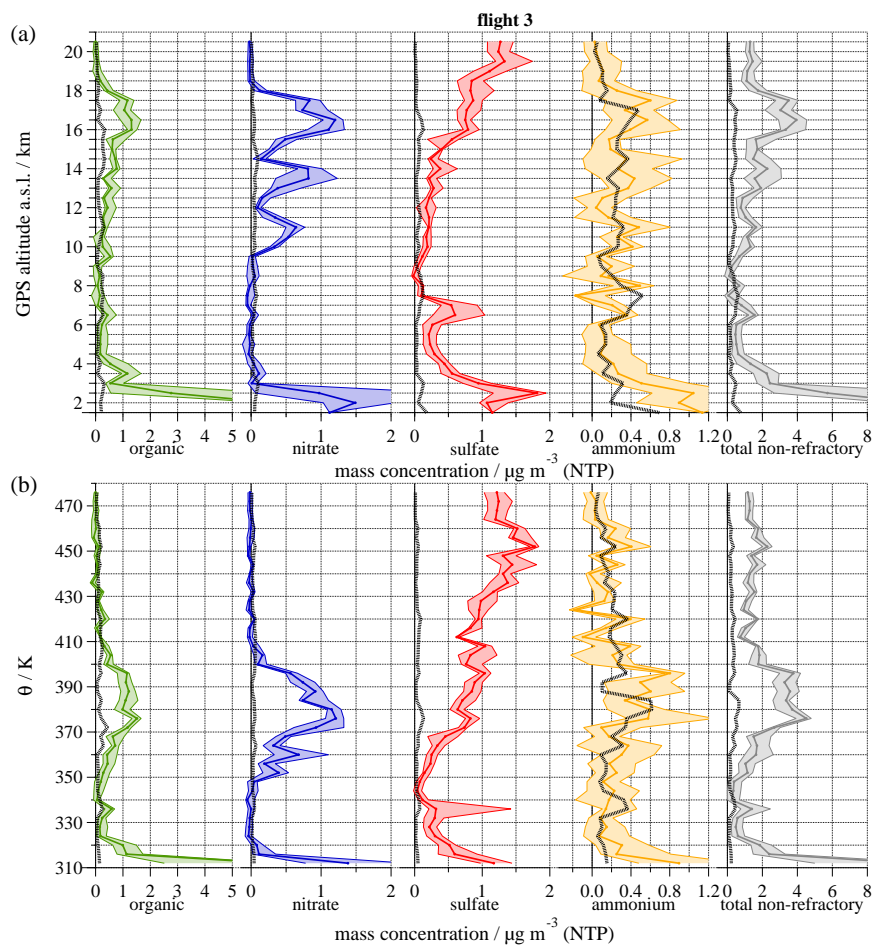
Figure S4. ERICA-AMS mass concentrations of particulate organics (green), nitrate (blue), sulfate (red), and ammonium (NH_4, orange) as a function of (a) GPS altitude and (b) potential temperature θ measured during research flight 3 on 31 July. The thick line and the shaded area represent the median and $25th/75th$ percentiles in the corresponding altitude or θ bin. The right panel displays the sum of all species measured by the ERICA-AMS (grey). For each altitude bin the detection limit is displayed as a dotted line.
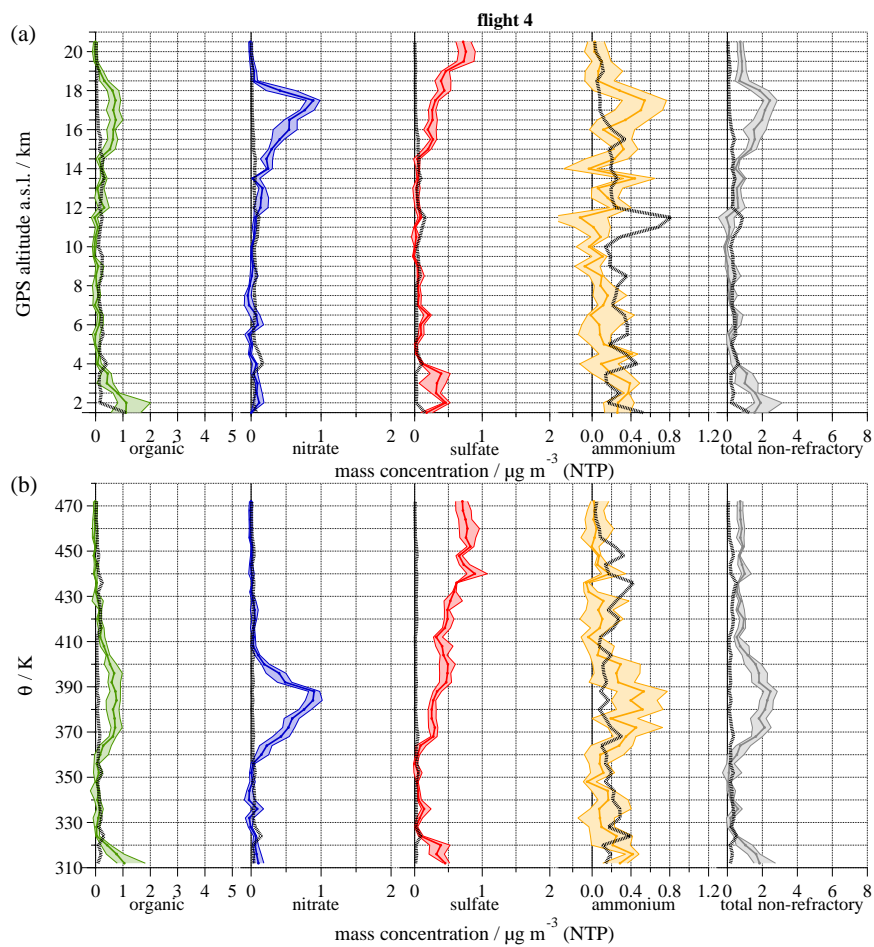
Figure S5. ERICA-AMS mass concentrations of particulate organics (green), nitrate (blue), sulfate (red), and ammonium (NH_4, orange) as a function of (a) GPS altitude and (b) potential temperature θ measured during research flight 4 on 2 August. The thick line and the shaded area represent the median and $25th/75th$ percentiles in the corresponding altitude or θ bin. The right panel displays the sum of all species measured by the ERICA-AMS (grey). For each altitude bin the detection limit is displayed as a dotted line.
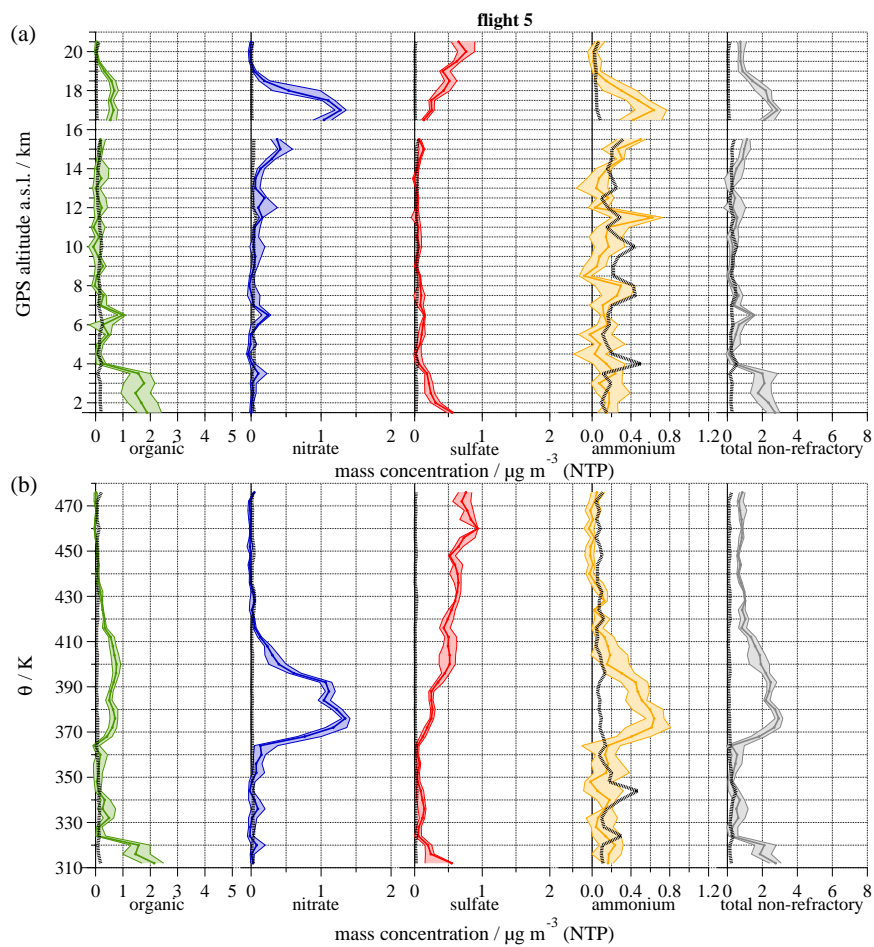
Figure S6. ERICA-AMS mass concentrations of particulate organics (green), nitrate (blue), sulfate (red), and ammonium (NH_4, orange) as a function of (a) GPS altitude and (b) potential temperature θ measured during research flight 5 on 4 August. The thick line and the shaded area represent the median and $25th/75th$ percentiles in the corresponding altitude or θ bin. The right panel displays the sum of all species measured by the ERICA-AMS (grey). For each altitude bin the detection limit is displayed as a dotted line.
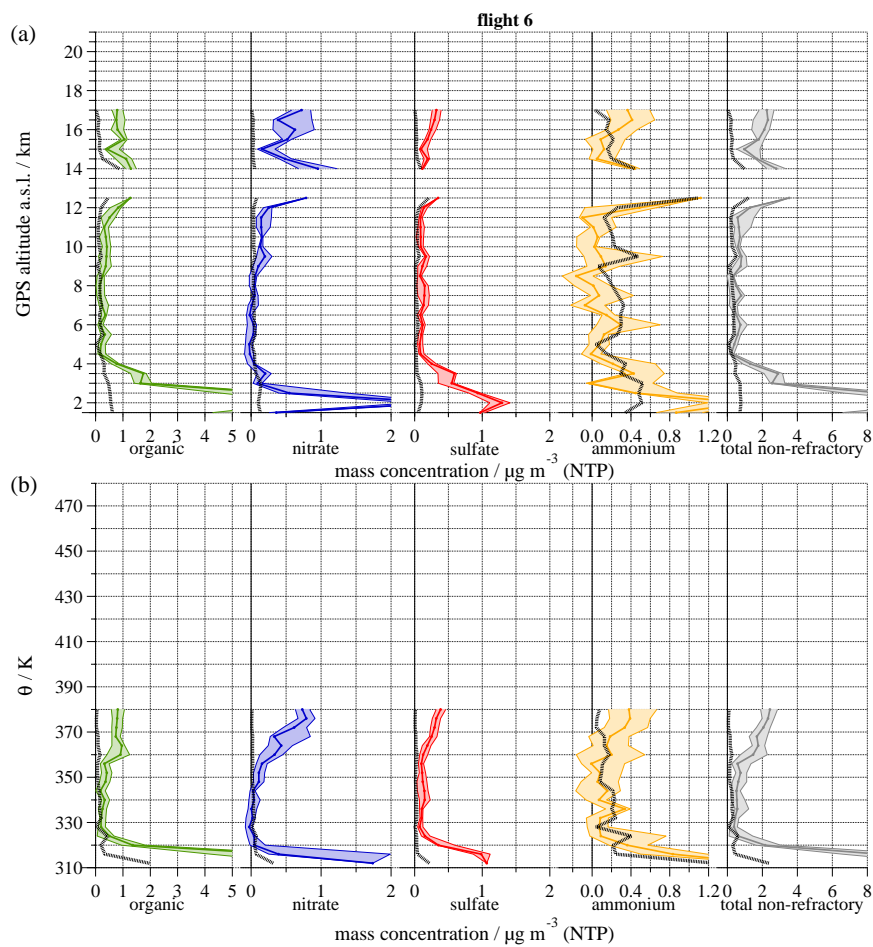
Figure S7. ERICA-AMS mass concentrations of particulate organics (green), nitrate (blue), sulfate (red), and ammonium (NH_4, orange) as a function of (a) GPS altitude and (b) potential temperature θ measured during research flight 6 on 6 August. The thick line and the shaded area represent the median and $25th/75th$ percentiles in the corresponding altitude or θ bin. The right panel displays the sum of all species measured by the ERICA-AMS (grey). For each altitude bin the detection limit is displayed as a dotted line.
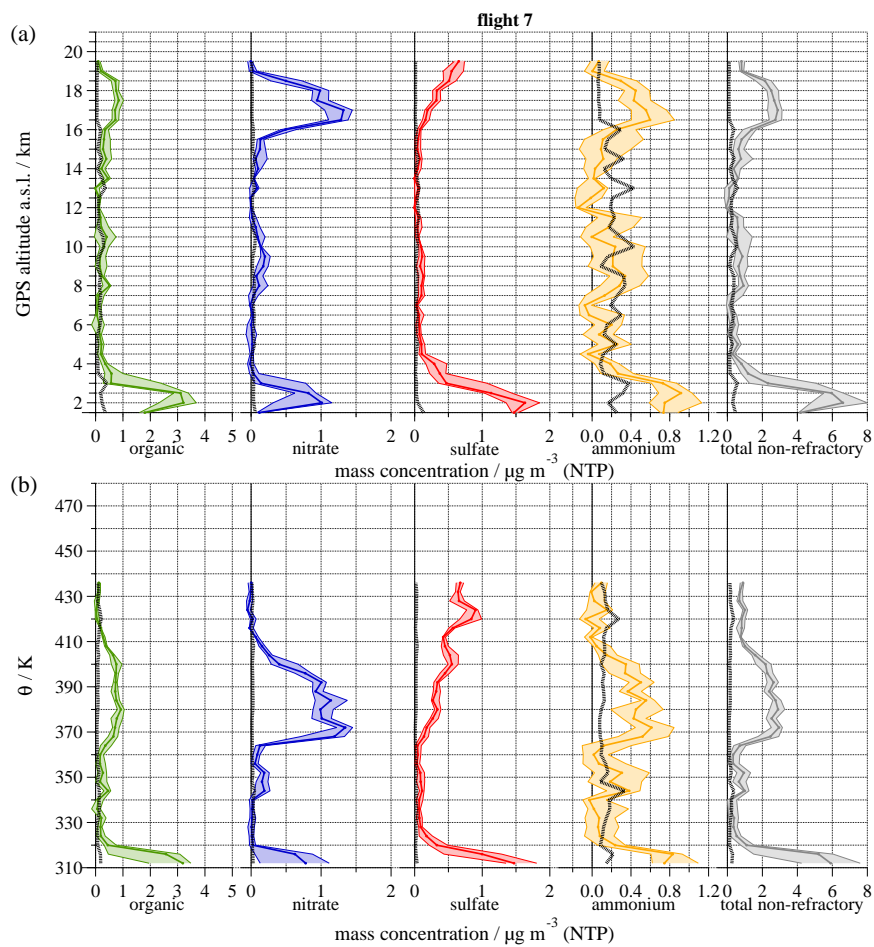
Figure S8. ERICA-AMS mass concentrations of particulate organics (green), nitrate (blue), sulfate (red), and ammonium (NH_4, orange) as a function of (a) GPS altitude and (b) potential temperature θ measured during research flight 7 on 8 August. The thick line and the shaded area represent the median and $25th/75th$ percentiles in the corresponding altitude or θ bin. The right panel displays the sum of all species measured by the ERICA-AMS (grey). For each altitude bin the detection limit is displayed as a dotted line.
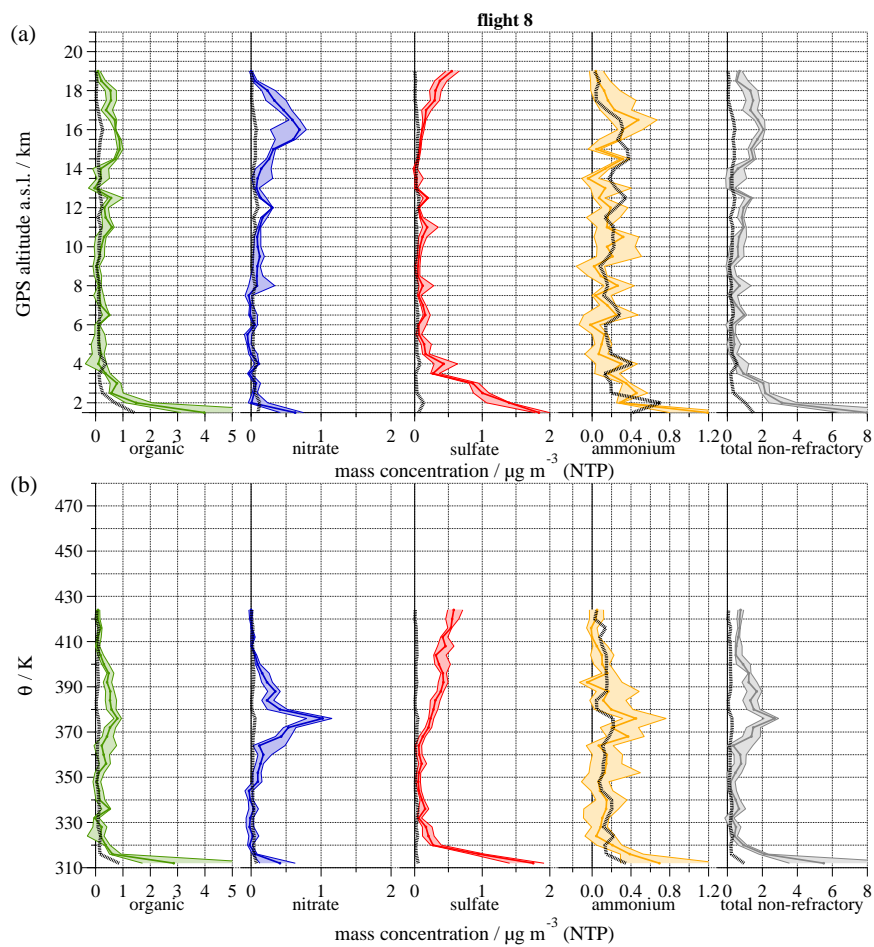
Figure S9. ERICA-AMS mass concentrations of particulate organics (green), nitrate (blue), sulfate (red), and ammonium (NH$_4$, orange) as a function of (a) GPS altitude and (b) potential temperature θ measured during research flight 8 on 10 August. The thick line and the shaded area represent the median and $25th/75th$ percentiles in the corresponding altitude or θ bin. The right panel displays the sum of all species measured by the ERICA-AMS (grey). For each altitude bin the detection limit is displayed as a dotted line.

References

Allan, J. D., Alfarra, M. R., Bower, K. N., Williams, P. I., Gallagher, M. W., Jimenez, J. L., McDonald, A. G., Nemitz, E., Cana-
garatna, M. R., Jayne, J. T., Coe, H., and Worsnop, D. R.: Quantitative sampling using an Aerodyne aerosol mass spectrometer
2. Measurements of fine particulate chemical composition in two U.K. cities, Journal of Geophysical Research: Atmospheres, 108,
https://doi.org/https://doi.org/10.1029/2002JD002359, https://agupubs.onlinelibrary.wiley.com/doi/abs/10.1029/2002JD002359, 2003a.

Allan, J. D., Jimenez, J. L., Williams, P. I., Alfarra, M. R., Bower, K. N., Jayne, J. T., Coe, H., and Worsnop, D. R.: Quantitative sam-
pling using an Aerodyne aerosol mass spectrometer 1. Techniques of data interpretation and error analysis, Journal of Geophysical
Research: Atmospheres, 108, https://doi.org/https://doi.org/10.1029/2002JD002358, https://agupubs.onlinelibrary.wiley.com/doi/abs/10.
1029/2002JD002358, 2003b.

Allan, J. D., Delia, A. E., Coe, H., Bower, K. N., Alfarra, M., Jimenez, J. L., Middlebrook, A. M., Drewnick, F., Onasch, T. B., Canagaratna,
M. R., Jayne, J. T., and Worsnop, D. R.: A generalised method for the extraction of chemically resolved mass spectra from Aerodyne
aerosol mass spectrometer data, Journal of Aerosol Science, 35, 909–922, https://doi.org/10.1016/j.jaerosci.2004.02.007, https://www.
sciencedirect.com/science/article/pii/S0021850204000229, 2004.

Bahreini, R., Jimenez, J. L., Wang, J., Flagan, R. C., Seinfeld, J. H., Jayne, J. T., and Worsnop, D. R.: Aircraft-based aerosol size and composi-
tion measurements during ACE-Asia using an Aerodyne aerosol mass spectrometer, Journal of Geophysical Research: Atmospheres, 108,
https://doi.org/https://doi.org/10.1029/2002JD003226, https://agupubs.onlinelibrary.wiley.com/doi/abs/10.1029/2002JD003226, 2003.

Drewnick, F., Hings, S. S., DeCarlo, P., Jayne, J. T., Gonin, M., Fuhrer, K., Weimer, S., Jimenez, J. L., Demerjian, K. L., Bor-
rmann, S., and Worsnop, D. R.: A New Time-of-Flight Aerosol Mass Spectrometer (TOF-AMS)—Instrument Description and First
Field Deployment, Aerosol Science and Technology, 39, 637–658, https://doi.org/10.1080/02786820500182040, https://doi.org/10.1080/
02786820500182040, 2005.

Drewnick, F., Hings, S. S., Alfarra, M. R., Prevot, A. S. H., and Borrmann, S.: Aerosol quantification with the Aerodyne Aerosol Mass Spec-
trometer: detection limits and ionizer background effects, Atmospheric Measurement Techniques, 2, 33–46, https://doi.org/10.5194/amt-
2-33-2009, https://amt.copernicus.org/articles/2/33/2009/, 2009.

Fry, J. L., Brown, S. S., Middlebrook, A. M., Edwards, P. M., Campuzano-Jost, P., Day, D. A., Jimenez, J. L., Allen, H. M., Ryerson,
T. B., Pollack, I., Graus, M., Warneke, C., de Gouw, J. A., Brock, C. A., Gilman, J., Lerner, B. M., Dubé, W. P., Liao, J., and Welti,
A.: Secondary organic aerosol (SOA) yields from NO_3 radical + isoprene based on nighttime aircraft power plant plume transects,
Atmospheric Chemistry and Physics, 18, 11 663–11 682, https://doi.org/10.5194/acp-18-11663-2018, https://acp.copernicus.org/articles/
18/11663/2018/, 2018.

Healy, R. M., O'Connor, I. P., Hellebust, S., Allanic, A., Sodeau, J. R., and Wenger, J. C.: Characterisation of single particles from in-port
ship emissions, Atmospheric Environment, 43, 6408–6414, https://doi.org/https://doi.org/10.1016/j.atmosenv.2009.07.039, https://www.
sciencedirect.com/science/article/pii/S1352231009006529, 2009.

Hinz, K. P., Greweling, M., Drews, F., and Spengler, B.: Data processing in on-line laser mass spectrometry of inorganic, organic, or biological
airborne particles, J. Am. Soc. Mass Spectrom., 10, 648–660, https://doi.org/10.1016/S1044-0305(99)00028-8, 1999.

Hünig, A., Appel, O., Dragoneas, A., Molleker, S., Clemen, H.-C., Helleis, F., Klimach, T., Köllner, F., Böttger, T., Drewnick, F.,
Schneider, J., and Borrmann, S.: Design, characterization, and first field deployment of a novel aircraft-based aerosol mass spectrom-
eter combining the laser ablation and flash vaporization techniques, Atmospheric Measurement Techniques Discussions, 2021, 1–43,
https://doi.org/10.5194/amt-2021-271, https://amt.copernicus.org/preprints/amt-2021-271/, 2021.

Klimach, T.: Chemische Zusammensetzung der Aerosole: Design und Datenauswertung eines Einzelpartikel-
Laserablationsmassenspektrometers, Ph.D. thesis, Johannes-Gutenberg Universität Mainz, 2012.

Köllner, F., Schneider, J., Willis, M. D., Klimach, T., Helleis, F., Bozem, H., Kunkel, D., Hoor, P., Burkart, J., Leaitch, W. R., Aliabadi, A. A.,
Abbatt, J. P. D., Herber, A. B., and Borrmann, S.: Particulate trimethylamine in the summertime Canadian high Arctic lower troposphere,
Atmos. Chem. Phys., 17, 13 747–13 766, https://doi.org/10.5194/acp-17-13747-2017, 2017.

Köllner, F., Schneider, J., Willis, M. D., Schulz, H., Kunkel, D., Bozem, H., Hoor, P., Klimach, T., Helleis, F., Burkart, J., Leaitch, W. R.,
Aliabadi, A. A., Abbatt, J. P. D., Herber, A. B., and Borrmann, S.: Chemical composition and source attribution of sub-micrometre aerosol
particles in the summertime Arctic lower troposphere, Atmospheric Chemistry and Physics, 21, 6509–6539, https://doi.org/10.5194/acp-
21-6509-2021, https://acp.copernicus.org/articles/21/6509/2021/, 2021.

Middlebrook, A. M., Bahreini, R., Jimenez, J. L., and Canagaratna, M. R.: Evaluation of Composition-Dependent Collection Ef-
ficiencies for the Aerodyne Aerosol Mass Spectrometer using Field Data, Aerosol Science and Technology, 46, 258–271,
https://doi.org/10.1080/02786826.2011.620041, https://doi.org/10.1080/02786826.2011.620041, 2012.

Moffet, R. C. and Prather, K. A.: In-situ measurements of the mixing state and optical properties of soot with implications for radiative
forcing estimates, P. Natl. Acad. Sci., 106, 11 872–11 877, https://doi.org/10.1073/pnas.0900040106, 2009.

230 Ng, N. L., Canagaratna, M. R., Zhang, Q., Jimenez, J. L., Tian, J., Ulbrich, I. M., Kroll, J. H., Docherty, K. S., Chhabra, P. S., Bahreini, R., Murphy, S. M., Seinfeld, J. H., Hildebrandt, L., Donahue, N. M., DeCarlo, P. F., Lanz, V. A., Prévôt, A. S. H., Dinar, E., Rudich, Y., and Worsnop, D. R.: Organic aerosol components observed in Northern Hemispheric datasets from Aerosol Mass Spectrometry, Atmospheric Chemistry and Physics, 10, 4625–4641, https://doi.org/10.5194/acp-10-4625-2010, https://acp.copernicus.org/articles/10/4625/2010/, 2010.

Ng, N. L., Canagaratna, M. R., Jimenez, J. L., Chhabra, P. S., Seinfeld, J. H., and Worsnop, D. R.: Changes in organic aerosol composition
235 with aging inferred from aerosol mass spectra, Atmos. Chem. Phys., 11, 6465–6474, https://doi.org/10.5194/acp-11-6465-2011, 2011.

Reitz, P.: Chemical composition measurements of cloud condensation nuclei and ice nuclei by aerosol mass spectrometry, Ph.D. thesis, Johannes Gutenberg-Universität Mainz, 2011.

Roth, A.: Untersuchungen von Aerosolpartikeln und Wolkenresidualpartikeln mittels Einzelpartikel-Massenspektrometrie und optischen Methoden, Ph.D. thesis, Johannes Gutenberg-Universität Mainz, 2014.

240 Roth, A., Schneider, J., Klimach, T., Mertes, S., van Pinxteren, D., Herrmann, H., and Borrmann, S.: Aerosol properties, source identification, and cloud processing in orographic clouds measured by single particle mass spectrometry on a central European mountain site during HCCT-2010, Atmos. Chem. Phys., 16, 505–524, https://doi.org/10.5194/acp-16-505-2016, 2016.

Savitzky, A. and Golay, M. J. E.: Smoothing and Differentiation of Data by Simplified Least Squares Procedures, Analytical Chemistry, 36, 1627–1639, https://doi.org/10.1021/ac60214a047, https://doi.org/10.1021/ac60214a047, 1964.

245 Schneider, J., Weigel, R., Klimach, T., Dragoneas, A., Appel, O., Hünig, A., Molleker, S., Köllner, F., Clemen, H.-C., Eppers, O., Hoppe, P., Hoor, P., Mahnke, C., Krämer, M., Rolf, C., Grooß, J.-U., Zahn, A., Obersteiner, F., Ravegnani, F., Ulanovsky, A., Schlager, H., Scheibe, M., Diskin, G. S., DiGangi, J. P., Nowak, J. B., Zöger, M., and Borrmann, S.: Aircraft-based observation of meteoric material in lower-stratospheric aerosol particles between 15 and 68° N, Atmospheric Chemistry and Physics, 21, 989–1013, https://doi.org/10.5194/acp-21-989-2021, https://acp.copernicus.org/articles/21/989/2021/, 2021.

250 Schulz, C.: Secondary organic aerosol in the pristine Amazonian atmosphere: chemical properties, formation pathways, and interactions with clouds, Ph.D. thesis, Johannes Gutenberg-Universität Mainz, 2019.

Schulz, C., Schneider, J., Amorim Holanda, B., Appel, O., Costa, A., de Sá, S. S., Dreiling, V., Fütterer, D., Jurkat-Witschas, T., Klimach, T., Knote, C., Krämer, M., Martin, S. T., Mertes, S., Pöhlker, M. L., Sauer, D., Voigt, C., Walser, A., Weinzierl, B., Ziereis, H., Zöger, M., Andreae, M. O., Artaxo, P., Machado, L. A. T., Pöschl, U., Wendisch, M., and Borrmann, S.: Aircraft-based observations
255 of isoprene-epoxydiol-derived secondary organic aerosol (IEPOX-SOA) in the tropical upper troposphere over the Amazon region, Atmospheric Chemistry and Physics, 18, 14 979–15 001, https://doi.org/10.5194/acp-18-14979-2018, https://acp.copernicus.org/articles/18/14979/2018/, 2018.

Siddiqui, S.: Studies of electrical properties of microchannel plates during and after high-temperature vacuum bakeout, IEEE Transactions on Electron Devices, 26, 1059–1064, https://doi.org/10.1109/T-ED.1979.19545, 1979.

260 Slater, D. C. and Timothy, J. G.: Microchannel plate modal gain variations with temperature, Review of Scientific Instruments, 64, 430–435, https://doi.org/10.1063/1.1144212, https://doi.org/10.1063/1.1144212, 1993.

Zanatta, M., Bozem, H., Köllner, F., Hoor, P., Schneider, J., Petzold, A., Bundke, U., Hayden, K., Staebler, R., Schulz, H., and Herber, A. B.: Airborne survey of trace gas and aerosol over the Southern Baltic Sea: from clean marine boundary layer to shipping corridor effect, submitted to Tellus B, 2019.

265 Ziegler, H.: Properties of Digital Smoothing Polynomial (DISPO) Filters, Appl. Spectrosc., 35, 88–92, http://www.osapublishing.org/as/abstract.cfm?URI=as-35-1-88, 1981.